

A New Nickel/cobalt Borate as High-Performance Anode Material for Sodium-Ion Batteries

Beibei Xu,^[a, b] Yongjie Cao,^{*[c]} Jie Xu,^[d] Deqiang Zhao,^[e] Nan Wang,^[c] and Baofeng Wang^{*[a]}

Sodium-ion batteries (SIBs) are widely considered a promising option for large-scale energy storage, but their energy density is limited by the low specific capacity anode material. Herein, we synthesize a compound, namely $\text{Co}_2\text{Ni}(\text{BO}_3)_2$ (denoted as CNBO), which is firstly served as an anode material in SIBs. The in-situ X-ray diffraction (XRD) and ex-situ X-ray photoelectron spectroscopy (XPS) are conducted to elucidate the Na-ion storage mechanism, which involves a conversion reaction with a theoretical specific capacity of 546 mAh g^{-1} . As anode material

for SIBs, CNBO exhibits a high initial reversible specific capacity of 544.2 mAh g^{-1} and maintains good cycling performance (319.2 mAh g^{-1} for 80 cycles at 0.2 A g^{-1}) with remarkable rate capabilities (235.3 mAh g^{-1} at 2 A g^{-1}). Furthermore, a sodium-ion full cell using CNBO as the anode and $\text{Na}_3\text{V}_2(\text{PO}_4)_3$ as the cathode (CNBO || NVP) can attain a maximum energy density of 146 Wh kg^{-1} with excellent cycle stability and rate capabilities. This work presents the possibilities for developing metal borate-based materials for efficient sodium-ion storage.

Introduction

The challenge of meeting the world's energy demands while simultaneously addressing environmental concerns remains a significant obstacle in today's global landscape. As a result, the advancement of renewable energy sources, such as solar and wind power, have been expedited in recent years.^[1–6] However, the intermittent and unstable nature of these energy sources necessitates the development of high-power density energy conversion and storage units.^[1,7–12] Sodium-ion batteries (SIBs) have been widely recognized as a promising candidate for large-scale energy storage due to the abundance of Na-element in nature and their relatively lower cost and safety.^[12–24] Thus, the high-capacity negative electrode materials are essential components in SIBs.^[1,14–18] Despite being widely used, graphite

anodes have a low theoretical capacity of only 31 mAh g^{-1} in ester electrolytes for sodium-ion storage.^[7,23] Therefore, it is imperative to develop anode materials with exceptional specific capacity and rate performance for achieving high-performance applications.

Metal borates are extensively researched due to their distinctive physical properties, encompassing nonlinear optical, electrical, piezoelectric, and semiconducting characteristics.^[24] Moreover, boron's pronounced lipophilicity led to a diverse array of polyborate anionic networks, encompassing BO_3^{3-} , BO_4^{5-} , and BO_6^{9-} . Consequently, this imparts metal borates with a wealth of structural diversity that can bestow a wide range of properties.^[23,24] In recent years, metal borates have garnered attention as anode materials for both lithium-ion batteries (LIBs) and SIBs, owing to their low cost, high specific capacity, and environmental friendliness.^[5,25–31] For instance, $\text{Ni}_3\text{B}_2\text{O}_6$ has demonstrated an initial charge capacity of 423.6 mAh g^{-1} at 100 mA g^{-1} for LIBs,^[27] while Fe_3BO_6 has exhibited a superior reversible capacity of 504.2 mAh g^{-1} at 400 mA g^{-1} for SIBs,^[5,6] as reported by Tian et al. These studies have inspired us to explore new borate-based anode materials with exceptional electrochemical performance for sodium-ion storage.

In this work, we synthesized the CNBO anode material via a solid-phase method and investigated the electrochemical performance in SIBs. The CNBO anode demonstrated impressive reversible capacity, robust long-term cycling stability, and remarkable rate capability. In order to further understand the electrochemical kinetics and the possible reason behind the smaller diffusion coefficient during the initial charge/discharge process, we conducted various tests including electrochemical impedance spectroscopy (EIS), in-situ X-ray diffraction (XRD), ex-situ X-ray photoelectron spectroscopy (XPS) and galvanostatic intermittent titration technique (GITT) tests. Additionally, we assembled a sodium-ion full cell (NCBO || NVP) to confirm its exceptional electrochemical performance. Overall, this work provides valuable insights into the potential application of novel metal borate anode materials in future SIBs.

[a] B. Xu, Prof. B. Wang

Shanghai Key Laboratory of Materials Protection and Advanced Materials in Electric Power, Shanghai University of Electric Power, Shanghai, 200090, People's Republic of China
E-mail: wangbaofeng@shiep.edu.cn

[b] B. Xu

State Key Laboratory of Functional Materials for Informatics, Shanghai Institute of Micro-System and Information Technology, Chinese Academy of Sciences, Shanghai, 200050, People's Republic of China

[c] Dr. Y. Cao, Dr. N. Wang

Department of Chemistry, Shanghai Key Laboratory of Molecular Catalysis and Innovative Materials, Institute of New Energy, Fudan University, Shanghai, 200433, People's Republic of China
E-mail: Yongjie_Cao@fudan.edu.cn

[d] Dr. J. Xu

School of Materials Science and Engineering, Anhui University of Technology, Ma'anshan, 243002, People's Republic of China

[e] Dr. D. Zhao

Key Laboratory of Hydraulic and Waterway Engineering and National Engineering Research Center for Inland Waterway Regulation, School of River & Ocean Engineering, Chongqing Jiaotong University, Chongqing, 400074, People's Republic of China

 Supporting information for this article is available on the WWW under <https://doi.org/10.1002/batt.202300241>

Results and Discussion

The structural characterizations of CNBO are presented in Figure 1. Figure 1(a) shows the Rietveld refined XRD spectrum of CNBO, which displays Bragg positions that match well with the orthorhombic lattice Pnnm space group and lattice constants $a=4.5053\text{ \AA}$, $b=5.447\text{ \AA}$ and $c=8.4074\text{ \AA}$, consistent with previous literature.^[32] The χ^2 value of 1.36% indicates that the successful attainment of pure-phase CNBO. The crystal structure of CNBO, depicted in the inset picture, reveals its crystallization in a kotoite structure and isostructural similarity with CNBO, and the crystal structure comprises two distinct types of Co/NiO₆ coordination octahedra and discrete trigonal BO₃ groups.^[32,33] The Fourier transform infrared spectrometer (FT-IR) spectrum of CNBO (Figure 1b) exhibits weak absorption bands at 3467 and 1637 cm⁻¹, which can be attributed to the O—H stretching and H—O—H bending modes of surface water adsorbed on the sample, respectively.^[27,34] The broad and strong bands observed at 1261 and 1206 cm⁻¹ are attributed to the asymmetric stretching of B—O bonds, while the characteristic peaks detected at 713 and 686 cm⁻¹ correspond to the out-of-plane bending mode of B—O bonds. Additionally, the in-plane

bending mode of B—O bonds is evidenced by the presence of peaks at 630 and 551 cm⁻¹. These spectroscopic results provide conclusive evidence for the existence of BO₃ groups within CNBO.^[32,35] Furthermore, the inductively coupled plasma (ICP) analysis demonstrated that the atomic ratios of Co, Ni, and B in the CNBO sample are 2.04:1:2.05, which aligns with the anticipated ratio for CNBO. The X-ray photoelectron spectroscopy (XPS) spectra in Figure 1(c–f) offer valuable insights into the elemental composition of CNBO, with the binding energies of all elements precisely calibrated against the C1s peak at 284.8 eV. The fitted Co 2p spectrum in Figure 1(c) exhibits prominent peaks at 780.6 eV (Co 2p_{3/2}) and 796.3 eV (Co 2p_{1/2}), accompanied by a shake-up satellite peak at 785.0 eV. Additionally, the peaks observed at 855.2 and 873.0 eV (Figure 1d) can be attributed to Ni 2p_{3/2} and Ni 2p_{1/2}, respectively, while the two sets of shake-up satellites located at around 860.5 and precisely at the energy of the Ni main lines are assigned to Ni's respective core levels. The B 1s peak (Figure 1e) is observed at 191.1 eV for CNBO, while the O 1s spectrum (Figure 1f) can be deconvoluted into three peaks: two corresponding to B—O (529.9 eV) and Ni/Co—O (531.3 eV), respectively, and a third attributed to physically and chemisorbed

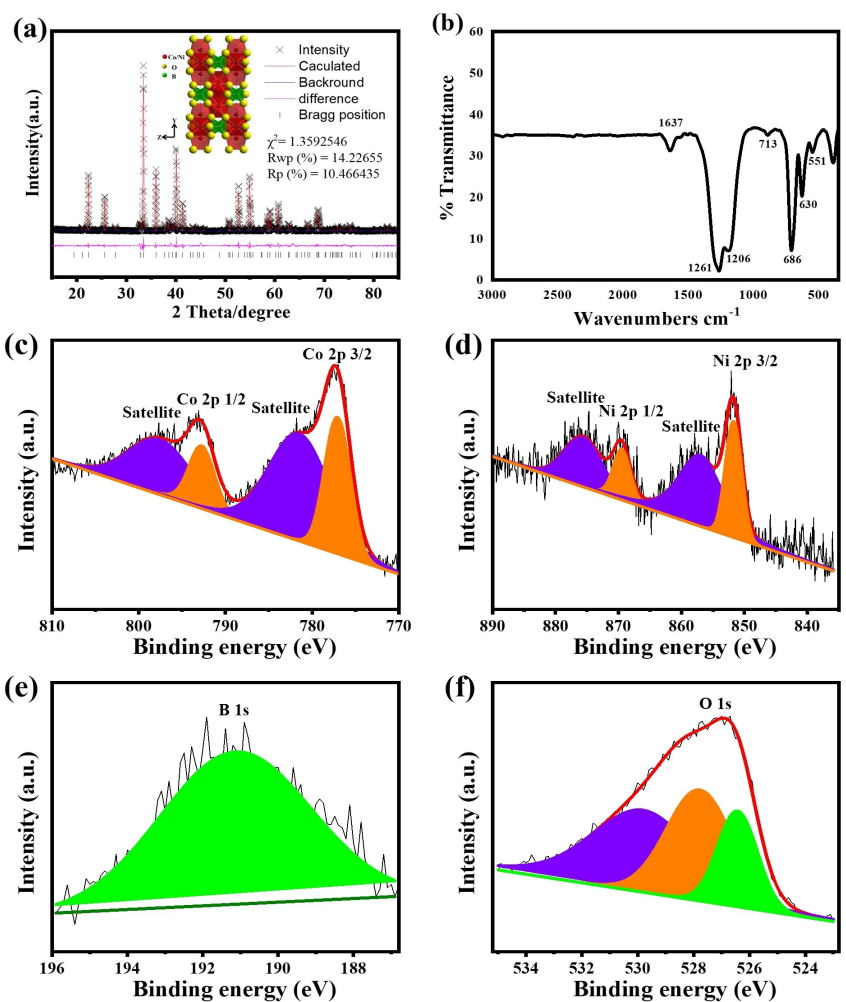


Figure 1. a) XRD Rietveld refinement pattern of CNBO and the inset was the corresponding crystal structure; b) FTIR Spectrum of CNBO; XPS spectra of c) Co 2p; d) Ni 2p; e) B 1s; f) O 1s.

water on the surface of CNBO at 533.3 eV. These findings are consistent with previous literature reports^[31,33,36–41] as well as FTIR results.

The field emission scanning electron microscopy (FE-SEM) and high-resolution transmission electron microscopy (HR-TEM) images of the CNBO sample are presented in Figure 2(a and b), revealing a size range spanning from sub-micron to micron scale. The HR-TEM, along with selected area electron diffraction (SAED) pattern shown in Figure 2(c and d), unequivocally confirms the single crystal structure of CNBO. Specifically, the HR-TEM image exhibits an interplanar spacing of 0.38 nm, corresponding precisely to the (101) plane as depicted in Figure 2(c). The SAED pattern depicted in Figure 2(d) reveals interplanar spacings of 0.38 nm and 0.28 nm for the (101) and (020) lattice planes, respectively. Additionally, the uniform dispersion of Co, Ni, B, and O elements is confirmed by spherical aberration transmission electron microscopy (STEM) image and energy dispersive spectrometer (EDS) mapping of CNBO powders in Figure 2(e–i). The Brunauer-Emmett-Teller (BET) specific surface area value is shown in Figure S1, which possesses a BET specific surface area value of 5.8 m² g⁻¹.

The Na-ion insertion/deinsertion processes in CNBO electrodes were investigated through the implementation of cyclic voltammetry (CV) tests (Figure 3a). During the initial cathodic scan, the first cycle exhibits redox peaks at 2.3 and 1.52 V, which subsequently vanish in subsequent scans due to the irreversible structural transformation of CNBO.^[5] A broad oxidation peak is observed in the anodic process at around 1.75 V. The subsequent cycles display broad reduction peaks at around 0.6 V, indicating good reversibility. Figure 3(b) illustrates the galvanostatic charge/discharge curves of CNBO at a current density of 0.2 A g⁻¹. The initial charge capacity is 544.2 mAh g⁻¹, accompanied by an initial Coulombic efficiency of 60%

attributed to the formation process of a solid-state interphase (SEI) film and the irreversible conversion reaction process of CNBO during the initial discharge.^[31,42] These curves for the next two cycles almost overlap, suggesting good reversibility, consistent with the results from the CV observation. Figure 3(c) showed the cycle life of CNBO at 0.2 A g⁻¹ in SIBs, where the CNBO electrode maintained 319.2 mAh g⁻¹ for 80 cycles. Even at 2 A g⁻¹, it exhibits a reversible specific capacity of 235.3 mAh g⁻¹ with a capacity retention ratio of 90% after 500 cycles (Figure S2a). However, more obvious capacity fading was observed after 80 cycles. The results of the rate capacities of CNBO anode over the current density range of 0.2–2 A g⁻¹ are displayed in Figure 3(d). The corresponding capacities at current densities of 0.2, 0.5, 1, and 2 A g⁻¹ were 452.3, 349.6, 308.5, and 235.3 mAh g⁻¹, respectively. The electrochemical performance of CNBO anode at different mass loading was shown in Figure S2(b), which indicates that it still exhibits a capacity retention ratio of 90% at 12 mg cm⁻² than that at 5 mg cm⁻² under current density of 0.2 A g⁻¹ in SIBs. Additionally, the recoverability of CNBO's capacity is observed upon reduction of current density to 0.2 A g⁻¹. Figure 3(e) illustrates the electrochemical impedance spectroscopy (EIS) spectra of CNBO at selected cycles. The R_{ct} value of CNBO exhibits a slight increase from 82.18 Ω after the first cycle to 117.6 Ω after 50 cycles, followed by a further rise to 133.5 Ω after 80 cycles. Additionally, the kinetics of sodium storage in the CNBO electrodes are investigated by GITT measurements. The equation^[10,43] is used to estimate the diffusivity of Na⁺ in CNBO using GITT data. The equation is as follows:

$$D_{\text{Li}^+} = \frac{4}{\pi\tau} \left(\frac{m_B V_M}{M_B A} \right)^2 \left(\frac{\Delta E_s}{\Delta E_t} \right)^2 \left(\tau \ll \frac{L^2}{D} \right)$$

Here, the active mass and molecular mass of CNBO are represented by m_B and M_B , respectively. V_M denotes the molar volume, A represents the area of the electrode, and L signifies the average radius of the electrode. ΔE_s indicates the voltage drop between the initial and steady state, while ΔE_t refers to the difference in voltage during a discharge pulse. According to our calculations, the profiles of the Na⁺ diffusion coefficients (D_{Na^+}) ranged from 4.02×10^{-15} to 1.18×10^{-11} cm² s⁻¹ during the first two cycles, as shown in Figure 3(f). The D_{Na^+} of the second cycle (1.765×10^{-12} cm² s⁻¹) is higher than that of the first cycle (1.153×10^{-12} cm² s⁻¹), and the D_{Na^+} of the first discharge process (5.62×10^{-13} cm² s⁻¹) is lower than that of the charge (21.31×10^{-13} cm² s⁻¹). The decrease in diffusion coefficient during discharge can be attributed to phase transition.^[43] Further mechanistic studies are currently underway in our laboratory.

To gain insight into the Na-ion storage mechanisms of CNBO electrodes, in-situ XRD analysis is conducted to examine the relationship between crystal structure evolution. The results are presented in Figure 4(a, b), which depict the in-situ XRD patterns during the initial discharge-charge process. As shown in Figure 4(b), the CNBO peaks, locate at approximately 33.6° and 40.2° (corresponding to (200) and (211) lattice planes), nearly vanish after discharging to 0.01 V, indicating an amorph-

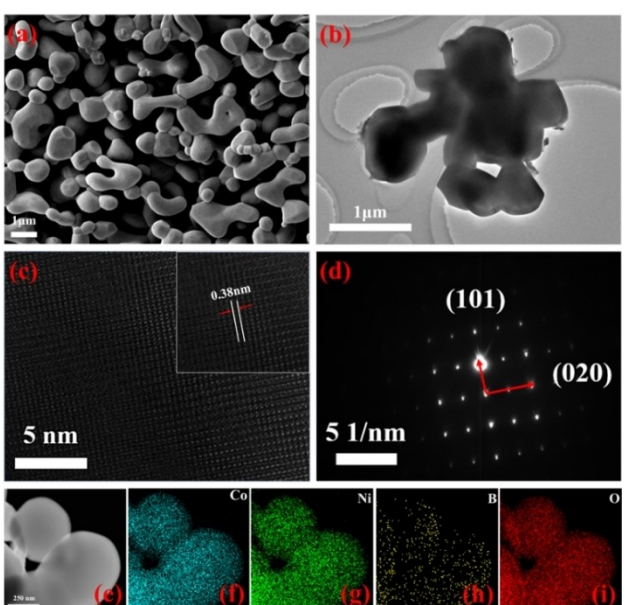


Figure 2. a, b) FE-SEM and TEM images of CNBO samples; c) HR-TEM images of CNBO samples; d) The SAED patterns of CNBO samples; e–i) STEM image and its corresponding EDS mappings (Co, Ni, B, and O).

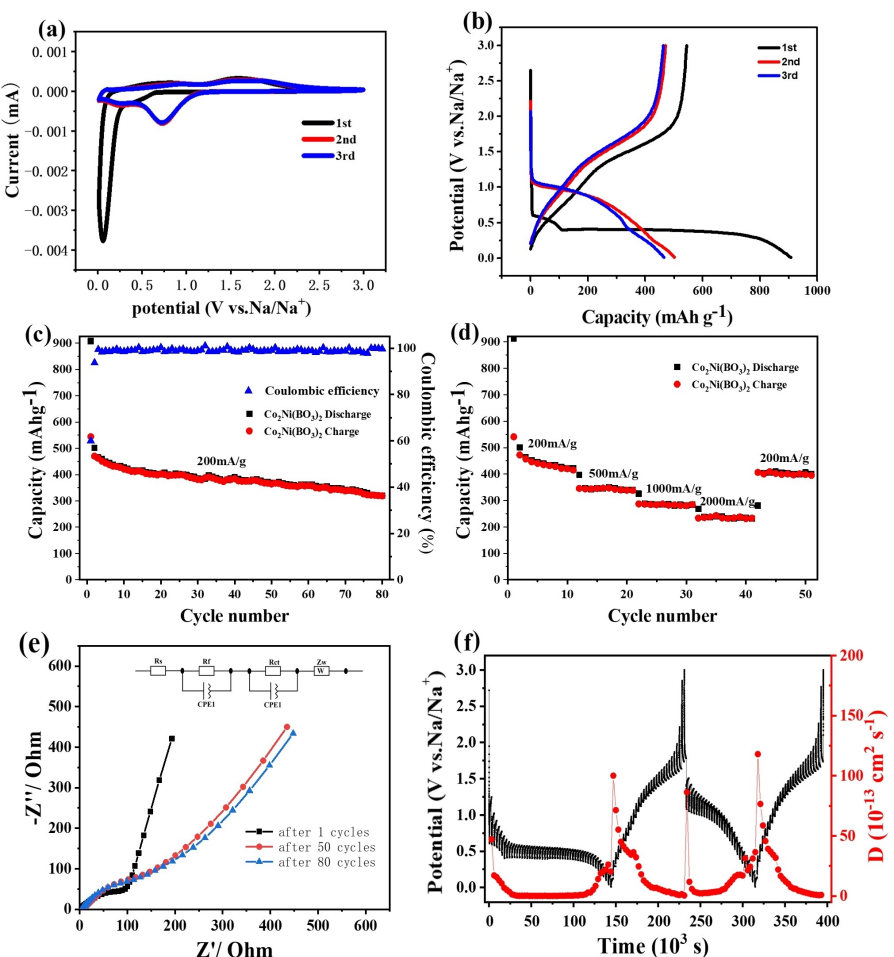


Figure 3. Electrochemical performance of CNBO anode for SIBs: a) Cyclic voltammetry curves at scan rate 0.2 mV s^{-1} ; b) initial three discharge/charge profiles of CNBO at 0.2 A g^{-1} ; c) cyclic performances of CNBO at a current density of 0.2 A g^{-1} ; d) rate capability of CNBO anode; e) EIS spectra for CNBO electrode (inset: equivalent circuit); f) GITT curves and the corresponded apparent Na-ion diffusion coefficients of CNBO in Na-ion battery as a function of time in the voltage range of $0.01\text{--}3.0 \text{ V}$.

ization process. The lattice planes (200) and (211) are also depicted in Figure 4(c), illustrating a gradual decrease in the intensity of diffraction peaks until they completely disappear upon initial discharge to 0.01 V . When charged to 3 V , these diffraction peaks remain in a state of disappearance. Interestingly, the CNBO peaks almost completely vanish in the fully discharged state, which can be attributed to the electrochemical formation of an undetectable product by XRD. Moreover, it is worth noting that the laboratory X-ray diffraction imposes a limitation on the intensity of diffraction peaks during *in situ* XRD experiments.

The ex-situ XPS measurements are conducted to investigate the valence changes of Co, Ni, O, and B elements before and during the initial charge/discharge process of the CNBO electrode. Figure 5(a) illustrates the Ni 2p spectrum, which can be further categorized into two primary peaks corresponding to Ni 2p_{1/2} and Ni 2p_{3/2} orbitals. After fitting using the Casa2318PR software, the Ni 2p_{3/2} spectrum of the original electrode exhibits a binding energy peak at 855.9 eV , indicating the presence of Ni^{2+} state.^[44] During the initial discharge process, there is a shift in the binding energy peak to a lower

location of 855.1 eV . Similarly, during the initial charge process, the binding energy peak reverts back to 855.4 eV . The results suggest that Ni exhibits reversible redox behavior during the charge/discharge process, while the Co 2p spectrum (Figure 5b) shows a binding energy peak at 781.0 eV in the initial electrode. When discharged to 0.01 V , the binding energy peak location shifts to a lower value of 779.4 eV , and after charging to 3.0 V , the location of the binding energy peak shifts back to 780.2 eV . The O 1s spectrum is depicted in Figure 5(c), with the binding energy peak situated at an original electrode position of 532.7 eV . During the discharge process, the binding energy peak undergoes a downward shift, indicating the conversion of CNBO to B_2O_3 (531.0 eV) and Na_2O (528.6 eV). Upon charged to 3 V , the binding energy of B_2O_3 remains unchanged while that of Na_2O disappears, giving rise to a new binding energy at 532.6 eV . This observation corresponds to the transformation from Na_2O to CoO and NiO . The B 1s spectrum in Figure 5(d) reveals a shift in binding energy from 192.1 to 191.7 eV , indicating the transformation of the original electrode into B_2O_3 during discharge at 0.01 V . Upon charged to 3 V , the binding energy remains nearly unchanged, suggesting the stable

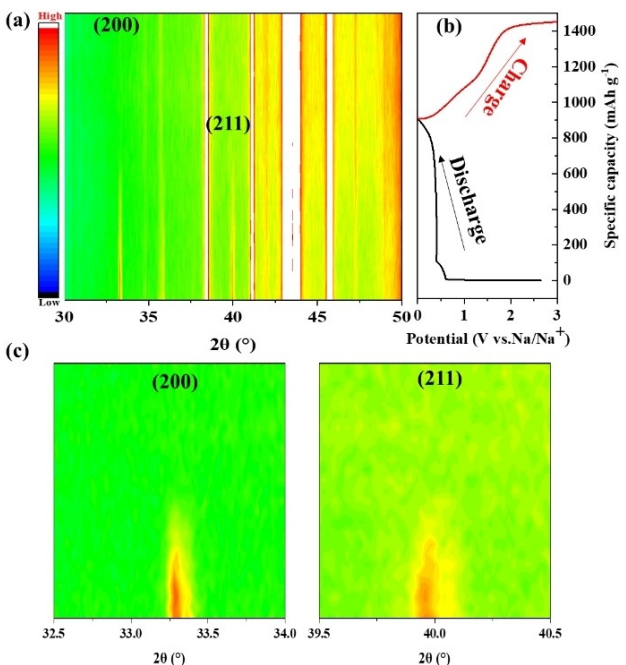
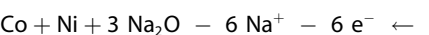
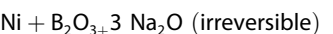
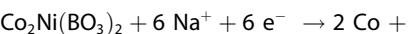


Figure 4. In situ XRD 2D contour plots of the CNBO electrode against the discharge/charge profile during the initial cycle.

presence of B_2O_3 . The Na-ion storage mechanism of CNBO electrode can be described by two reactions.



Based on the in situ XRD analysis, CNBO anode material exhibits a reversible insertion/desertion of six sodium ions, resulting in a theoretical capacity of 546 mAh g^{-1} . The Na-ion storage mechanism involves a typical conversion reaction described by Equation (1), where CNBO is converted to Co, Ni, B_2O_3 and Na_2O during initial discharge. Conversely, charging leads to the reaction between Co, Ni and Na_2O producing CoO and NiO as shown in equation (2). The SEM images and corresponding photos of the CNBO electrode pre- and post-cycling are presented in Figure S2. The pristine electrode exhibited a relatively smooth surface (Figure S3a–c), while after 10 cycles, numerous cracks were observed on the surface (Figure S3d–f). Obvious pulverizations were visible in Figure S3(g–i), further confirming the in situ XRD results.

The sodium-ion full cell is assembled using carbon-coated $\text{Na}_3\text{V}_2(\text{PO}_4)_3$ (referred to as NVP) as the cathode and pre-sodified CNBO as the anode. Details of the pre-sodification process for CNB are provided in the Experiment Section of the Supporting Information. The XRD pattern of prepared NVP, shown in Figure S4(a), indicates its purity. Initial charge/discharge curves of NVP, presented in Figure S4(b), demonstrate a reversible specific capacity of 105 mAh g^{-1} with a corresponding coulom-

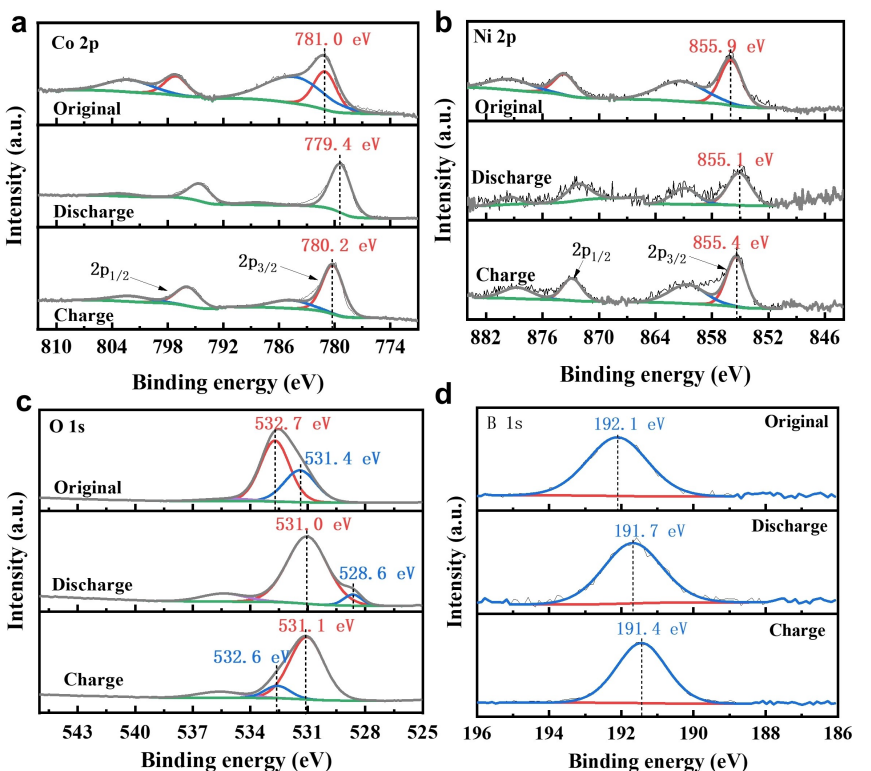


Figure 5. The ex-situ XPS of CNBO; a) the Ni 2p spectrum of CNBO electrode; b) the Co 2p spectrum of CNBO electrode; c) O 1s spectrum of CNBO electrode; d) the B 1s spectrum of CNBO electrode.

bic efficiency of 98%. The mass loading ratio between negative and positive (N/P) is 1:5.3 and the amount of electrolyte adding is 10 g per Ah in the full cell. The first to third charge/discharge curves of the CNBO||NVP sodium-ion full cell are shown in Figure 6(b), demonstrating a reversible specific capacity of 80 mAh g⁻¹ at 0.1 C (based on the total electrode material mass). The rate capability of the CNBO||NVP sodium-ion full cell (Figure 6c) demonstrates a reversible specific capacity of 80, 75, 70, 60, 50, and 48 mAh g⁻¹ at 0.1, 0.2, 0.5, 1.0, 2.0, and 5.0 C, respectively. Figure 6(d) illustrates the cycle stability of the CNB||NVP sodium-ion full cell, which can cycle 100th with a capacity retention of 80% at 1 C. The Ragone plot of the CNBO||NVP sodium-ion full cell is shown in Figure S5, indicating a maximum specific energy/power density of 146 Wh kg⁻¹ and 193 W kg⁻¹ (based on total active materials), respectively.

Conclusions

A high-performance anode for SIBs is produced using a simple solid-state process to fabricate CNBO material. The negative electrode of CNBO demonstrates an impressive charge capacity of 544.2 mAh g⁻¹ and delivers 319.2 mAh g⁻¹ after 80 cycles as an anode for SIBs. Even at a high current density of 2 A g⁻¹, the CNBO anode material maintains a remarkable Na-ion storage performance with a capacity of 235.3 mAh g⁻¹. The in-situ XRD and ex-situ XPS results indicate that the electrochemical

reaction mechanism involves a conversion reaction based on the reversible redox reactions of Ni²⁺/Ni and Co²⁺/Co. The kinetics study of EIS demonstrate excellent rate capability, and GITT reveal that the smaller diffusion coefficient observed during the first discharge process is likely attributed to the phase transition occurring in the CNBO material used as anode material for SIBs. Furthermore, the CNBO||NVP sodium-ion full cell exhibits a maximum energy density of 146 Wh kg⁻¹ and maintains exceptional cycle stability and rate capabilities. These results underscore the potential applicability of metal borates, particularly CNBO, as anodes for SIBs.

Experimental Section

Materials preparation

All those reagents are analytical reagent (AR) without further treatment. The CNBO material is synthesized using a conventional solid-state method with analytical grade chemicals purchased from Macklin Company without any purification. Co(NO₃)₂·6H₂O, Ni(NO₃)₂·6H₂O, and H₃BO₃ are mixed in a molar ratio of 2:1:2.5 with an excess of 0.5 molar of boron. The mixture is ground and then heated in a muffle furnace at 900 °C for 48 h. The resulting CNBO powders are washed three times with 90 °C deionized water and dry overnight at 120 °C.

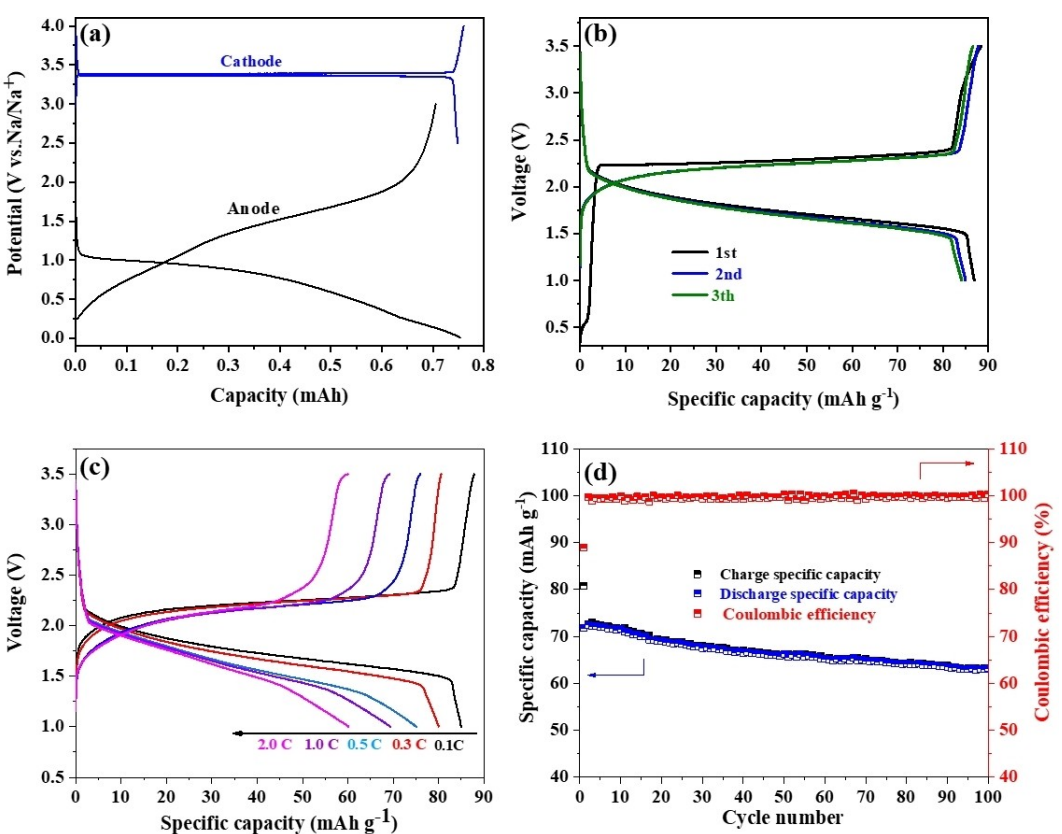


Figure 6. a) The charge/discharge curves of cathode/anode (CNBO/NVP) sodium-ion half-cell; b) the 1st–3rd charge/discharge curves of CNBO||NVP sodium-ion full cell; c) the rate capability of CNBO||NVP sodium-ion full cell; d) the cycle stability of CNBO||NVP sodium-ion full cell.

Materials characterization

The D/max-2000 instrument (Rigaku) is utilized to collect the X-ray diffraction (XRD) pattern, with a scanning rate of $0.2^\circ \text{ min}^{-1}$. The data is analyzed using a general structure analysis system (GSAS) software. The surface elemental states of the samples are studied using X-ray photoelectron spectroscopy (XPS, PHI-5700-ESCA). The ICP (Varian, 720-ES) is employed to detect the content of Ni, Co, and B. Fourier Transform Infrared (FT-IR) spectra is tested via an IRPrestige-21 SHIMADZU instrument, scanning between 400 and 4000 cm^{-1} . The JEM-7800F microscope is used to carry out FESEM observations, while a JEM-2100 microscope is utilized to perform TEM, HRTEM, SAED and EDS mapping measurements.

Electrochemical measurements

The working electrodes are prepared by mixing CNBO, carbon black, and carboxymethylcellulose sodium (CMC–Na) in a weight ratio of 80:10:10 in demineralized water. The resulting mixture is uniformly spread onto a Cu-foil with an average loading of approximately 5 mg cm^{-2} . Galvanostatic discharge/charge experiments are conducted using a Land-CT2001 A battery testing system over the voltage range of 0.01–3.0 V. For SIBs, sodium metal, the glass fiber film (Whatman), and a 1 mol L^{-1} NaClO_4 electrolyte in ethylene carbonate (EC), diethyl carbonate (DEC), and fluoroethylene carbonate (FEC) (in a volume ratio of 99.5:99.5:1) are used as the anode electrodes, separator (Whatman GF/C), and electrolyte, respectively. Cyclic voltammetry (CV) and electrochemical impedance spectroscopy (EIS) tests are conducted using an Autolab PGSTAT302. The CV tests were performed at a scan rate of 0.2 mV s^{-1} , and EIS is recorded over a frequency range of 100 kHz–10 MHz. All electrochemical measurements are carried out at room temperature.

Supporting Information

Supporting Information is available from the Wiley Online Library or from the author.

Acknowledgements

The authors appreciate support from the National Natural Science Foundation of China (No. 21673136, 22075173, 21875045 and 22005059). Science and Technology Commission of Shanghai Municipality (19DZ2270100, 19DZ1205500, 19DZ2271100 and 21010501100), The Natural Science Foundation of Chongqing (cstc2021jcyj-msxmX0912), The Science and Technology Research Program of Chongqing and Municipal Education Commission (KJQN202100739). Furthermore, the authors thank the support from the Shiyanjia Lab (www.shiyanjia.com).

Conflict of Interests

The authors declare no conflict of interest.

Data Availability Statement

Research data are not shared.

Keywords: energy storage • sodium-ion batteries • anode material • borate

- [1] C. L. Zhao, Q. D. Wang, Z. P. Yao, J. L. Wang, B. J. Sánchez-Lengeling, F. X. Din, X. G. Qi, Y. X. Lu, X. D. Bai, B. H. Li, H. L. A. Aspuru-Guzik, X. J. Huang, C. Delmas, M. Wagemaker, L. Q. Chen, Y. S. Hu, *Science* **2020**, *370*, 708–711.
- [2] Y. Q. Li, Q. Zhou, S. T. Weng, F. X. Ding, X. Qi, J. Z. Lu, Y. Li, X. Zhang, X. H. Rong, Y. X. Lu, X. F. Wang, R. J. Xiao, H. Li, X. J. Huang, L. Q. Chen, Y. S. Hu, *Nat. Energy* **2022**, *7*, 511–519.
- [3] Z. Y. Lu, C. N. Geng, H. J. Yang, P. He, S. C. Wu, Q. H. Yang, H. S. Zhou, *Proc. Natl. Academ. Sci.* **2022**, *119*, e2210203119.
- [4] H. Y. Lei, H. Wang, B. X. Cheng, F. Zhang, X. J. Liu, G. Wang, B. B. Wang, *Small* **2023**, *19*, 2206340.
- [5] J. Tian, B. Wang, F. Zhao, X. Ma, Y. Liu, H. K. Liu, Z. Huang, *Chem. Commun.* **2017**, *53*, 4698–4701.
- [6] Y. Liu, W. Li, Y. Xia, *Electrochim. Energy R.* **2021**, *4*, 447–472.
- [7] Y. J. Cao, X. L. Li, X. L. Dong, M. C. Liao, N. Wang, J. W. Cheng, J. Xu, Y. E. Q, Y. Liu, Y. Y. Xia, *Small* **2022**, *18*, 2204830.
- [8] M. H. Zhang, J. Ke Meng, N. Xiao, R. W. Shao, X. J. Wu, P. Gao, Z. Shadike, Y. N. Zhou, *Chem. Commun.* **2022**, *58*, 10345.
- [9] B. E. Murdock, K. E. Toghill, N. Tapia-Ruiz, *Adv. Energy Mater.* **2021**, *2102028*.
- [10] J. Li, X. Shi, J. Fang, J. Li, Z. Zhang, *ChemNanoMat.* **2016**, *2*, 997–1002.
- [11] J. Liang, C. Yuan, H. Li, K. Fan, Z. Wei, H. Sun, J. Ma, *Nano-Micro Lett.* **2018**, *10*, 21.
- [12] P. Li, X. Zheng, H. Yu, G. Zhao, J. Shu, X. Xu, W. Sun, S. X. Dou, *Energy Storage Mater.* **2019**, *16*, 512–518.
- [13] H. Li, K. Qian, X. Qin, D. Liu, R. Shi, A. Ran, C. Han, Y. B. He, F. Kang, B. Li, *J. Power Sources.* **2018**, *385*, 114–121.
- [14] C. Vaalma, D. Buchholz, M. Weil, S. Passerini, *Nat. Rev. Mater.* **2018**, *3*, 18013.
- [15] J. Y. Zhang, Z. Meng, D. Yang, K. M. Song, L. W. Mi, Y. P. Zhai, X. X. Guan, W. H. Chen, *J. Energy Chem.* **2022**, *68*, 27–34.
- [16] Y. H. Wan, K. M. Song, W. H. Chen, C. D. Qin, X. X. Zhang, J. Y. Zhang, H. L. Dai, Z. Hu, P. F. Yan, C. T. Liu, S. H. Sun, S. L. Chou, C. Y. Shen, *Angew. Chem. Int. Ed.* **2021**, *60*, 11481–11486.
- [17] X. Xu, J. Liu, Z. Liu, Z. Wang, R. Hu, J. Liu, L. Ouyang, M. Zhu, *Small* **2018**, *14*, 1800793.
- [18] X. Xu, S. Ji, M. Gu, J. Liu, *ACS Appl. Mater. Interfaces* **2015**, *7*, 20957–20964.
- [19] J. Liu, X. Xu, R. Hu, L. Yang, M. Zhu, *Adv. Energy Mater.* **2016**, *6*, 1600256.
- [20] T. Liu, N. Peng, X. Zhang, R. Zheng, M. Xia, J. Zhang, H. Yu, L. Zhang, J. Shu, *Energy Storage Mater.* **2021**, *42*, 42–67.
- [21] B. Wang, X. Zhang, X. Liu, G. Wang, H. Wang, J. Bai, *J. Colloid Interface Sci.* **2018**, *528*, 225–236.
- [22] A. Li, L. Xu, C. Li, Y. Q. Qian, *J. Mater. Chem. A* **2016**, *4*, 5489–5494.
- [23] F. Strauss, G. Rousse, M. T. Sougrati, D. A. Dalla Corte, M. Courty, R. Dominiko, J. M. Tarascon, *Inorg. Chem.* **2016**, *55*, 12775–12782.
- [24] B. Yang, H. Liu, R. Lv, H. Li, X. Fu, J. Su, X. Liu, W. Gu, *B. Chem. Soc. Jpn.* **2018**, *91*, 548–553.
- [25] B. Wu, S. Qi, X. Wu, H. Wang, Q. Zhuang, H. Yi, P. Xu, Z. Xiong, G. Shi, S. Chen, B. Wang, *Chin. Chem. Lett.* **2021**, *380*, 119935.
- [26] S. Li, L. Xu, G. Li, M. Wang, Y. Zhai, *J. Power Sources* **2013**, *236*, 54–60.
- [27] P. Liang, L. Du, X. Wang, Z.-H. Liu, *Solid State Sci.* **2014**, *37*, 131–135.
- [28] X. X. Shi, X. J. Liu, L. J. Yuan, *Adv. Mater. Res.* **2011**, *236*, 238.
- [29] B. Zhang, L. Ming, H. Tong, J.-F. Zhang, J. C. Zheng, X.-W. Wang, H. Li, L. Cheng, *J. Alloys Compd.* **2018**, *740*, 382–388.
- [30] C. Yongjie, C. Xinkle, D. Xiaoli, Z. Xiang, X. Jie, W. Nan, Y. Yang, W. Congxiao, L. Yao, X. Yongyao, *Adv. Funct. Mater.* **2021**, *31*, 2102856.
- [31] B. Xu, Y. Liu, J. Tian, X. Ma, Q. Ping, B. Wang, Y. Xia, *Chem. Eng. J.* **2019**, *363*, 285–291.
- [32] B. Tekin, H. Güler, *Mater. Chem. Phys.* **2008**, *108*, 88–91.
- [33] E. A. Turhan, S. V. K. Nune, E. Ulker, U. Sahin, Y. Dede, F. Karadas, *Chemistry* **2018**, *24*, 10372–10382.
- [34] X. Liu, W. Zhu, X. Cui, T. Liu, Q. Zhang, *Powder Technol.* **2012**, *222*, 160–166.
- [35] H. Güler, B. Tekin, *Inorg. Mater.* **2009**, *45*, 538–542.

- [36] F. Wang, H. Y. Zhuo, X. G. Han, W. Chen, D. Sun, *J. Mater. Chem. A* **2017**, *5*, 22964–22969.
- [37] Z. Fangcai, Z. Dequan, C. Qianwang, *ACS Appl. Mater. Interfaces* **2014**, *6*, 9256–9264.
- [38] V. Ragupathi, M. Safiq, P. Panigrahi, T. Hussain, S. Raman, R. Ahuja, G. S. Nagarajan, *Ionics* **2017**, *23*, 1645–1653.
- [39] P. Biswas, S. D. Baek, J. W. Kim, S. R. Cho, D. K. Kwon, S. J. Lee, J. M. Myoung, *Mater. Chem. Phys.* **2017**, *201*, 63–68.
- [40] S. K. Park, S. H. Yang, Y. C. Kang, *Chem. Eng. J.* **2018**, *349*, 214–222.
- [41] X. Zhang, Y. Zhou, Y. Mao, M. Wei, W. Chu, K. Huang, *Chem. Phys. Lett.* **2019**, *715*, 278–283.
- [42] X. Xu, Z. Liu, S. Ji, Z. Wang, Z. Ni, Y. Lv, J. Liu, J. Liu, *Chem. Eng. J.* **2019**, *359*, 765–774.
- [43] W. L. Pang, J. Z. Guo, X. H. Zhang, C. Y. Fan, X. J. Nie, H. Y. Yu, W. H. Li, Q. Yang, X. L. Wu, *J. Alloys Compd.* **2019**, *790*, 1092–1100.
- [44] F. Zheng, D. Zhu, Q. Chen, *ACS Appl. Mater. Interfaces* **2014**, *6*, 9256–9264.

Manuscript received: June 7, 2023
Revised manuscript received: August 3, 2023
Accepted manuscript online: August 10, 2023
Version of record online: September 8, 2023
